PAPER

Check for updates

In-plasma-catalysis for NO$_x$ degradation by Ti^{3+} self-doped TiO$_{2-x}$/γ-Al$_2$O$_3$ catalyst and nonthermal plasma

Xingdong Yang, Jiyan Qu, Linxi Wang and Jianhong Luo [ID] *

In an attempt to realize the efficient treatment of NO$_x$, a mixed catalyst of Ti^{3+} self-doped TiO$_{2-x}$ and γ-Al$_2$O$_3$ was constructed by reducing commercial TiO$_2$. The degradation effect on NO$_x$ was evaluated by introducing the mixed catalyst into a coaxial dual-dielectric barrier reactor. It was found that the synthesized TiO$_{2-x}$ could achieve considerable degradation effects (84.84%, SIE = 401.27 J L^{-1}) in a plasma catalytic system under oxygen-rich conditions, which were better than those of TiO$_2$ (73.99%) or a single plasma degradation process (26.00%). The presence of Ti^{3+} and oxygen vacancies in TiO$_{2-x}$ resulted in a relatively narrow band gap, which contributed to catalyzing deeply the oxidation of NO$_x$ to NO$_2^-$ and NO$_3^-$ during the plasma-induced "pseudo-photocatalysis" process. Meanwhile, the TiO$_{2-x}$ showed an improved discharge current and promoted discharge efficiency, explaining its significant activation effect in the reaction. Reduced TiO$_{2-x}$ could achieve an impressive degradation effect in a long-time plasma-catalysis process, and still maintained its intrinsic crystal structure and morphology. This work provides a facile synthesis procedure for preparing Ti^{3+} self-doped TiO$_{2-x}$ with practical and scalable production potential; moreover, the novel combination with plasma also provides new insights into the low-temperature degradation of NO$_x$.

1. Introduction

Since the 1980s, with rapid economic development, environmental problems derived from an excess of nitrogen sources[1] have become increasingly severe. As one of the important manifestations of excess nitrogen, NO$_x$ plays a key pollutant role in causing regional environmental problems such as acid rain, photochemical smog, and the greenhouse effect.[2] NO$_x$ pollution mainly arises from industrial production activities like the preparation of phosphoric acid using the nitric acid method,[3] which lead to much higher levels than the NO$_x$ produced in natural activities.[4] Therefore, there is an urgent need to implement more effective NO$_x$ degradation methods to achieve a sustainable development model.

Due to its milder operating conditions, low-temperature plasma can generate high-energy electrons to bombard heavy particles when the macroscopic temperature is close to normal temperature, realizing a reaction process that could only occur at high temperature and high pressure under traditional conditions.[5] NTP (non-thermal-plasma) has been widely used in present industrial production, pollution control and other fields, such as the surface etching of nano materials,[6] dust-containing gas dust removal,[7] high COD wastewater degradation,[8] *etc.* Research studies on the direct degradation of NO$_x$ by low-temperature plasma were

carried out as early as the 1990s,[9] but were hampered by a low degradation efficiency, poor target selectivity, and the creation of by-products causing secondary pollution.[10] With the aim of solving the above problems, the integration of heterogeneous catalysts with NTP and their subsequent synergistic effect have gradually become a current research hotspot.[11–14]

Low-temperature plasma-driven catalysis involves placing the catalyst in the discharge interval of the plasma reactor, wherein the catalyst could more directly utilize the high-energy electrons and active radicals generated during the plasma discharge process.[15] The degradation modes of NO$_x$ can be divided into reductive degradation[16] and oxidative degradation.[17] The reductive degradation of NO$_x$ often requires the introduction of olefinic reducing gases to achieve good degradation effects at high temperatures.[18,19] The application of N-type semiconductors in low-temperature plasma-driven catalysis has provided a new way to achieve oxidative degradation. Notably, a "pseudo-photocatalysis" behavior in the catalytic process is driven by the plasma, that is, the N-type semiconductor is activated by high-energy electrons in the plasma discharge interval, so that electron–hole pairs can be generated without a light source to degrade NO$_x$. Meanwhile, the nature of the catalyst can also affect the discharge characteristics in the plasma discharge process, thereby affecting or even changing the degradation path.[20] Therefore, the combination of the plasma and the embedded N-type semiconductor photocatalyst

Department of Chemical Engineering, Sichuan University, Chengdu, Sichuan 610065, P.R. China. E-mail: luojianhong@scu.edu.cn
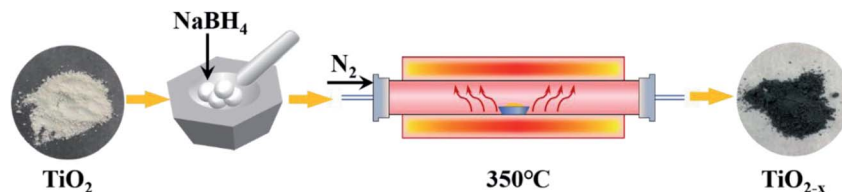
Fig. 1 Schematic diagram of the typical TiO_{2-x} preparation process.

can feasibly synergistically promote the high-efficiency degradation of NO_x.

TiO_2 is regarded as a promising N-type semiconductor catalyst for industrial applications using photocatalysis due to its advantages of low-toxicity, chemical and thermal stability, and corrosion resistance.[21,22] Chen et al.[23] revealed the relationship between the band gap of an N-type semiconductor and the NO_x degradation efficiency in the process of DBD (Dielectric Barrier Discharge) synergistic catalytic oxidation to remove NO_x, thus it is very important to find a simple and effective modification method for TiO_2. Recently, hydrogenated black titanium dioxide[24–26] has aroused widespread research interest due to its narrow band gap and high-efficiency full-spectrum response characteristics. The reduction of TiO_2 is different from the common modification methods of TiO_2 (non-metal doping[27–29] and noble metal doping[30–32]); herein abundant Ti^{3+} and oxygen vacancies was generated through Ti^{3+} self-doped method for reduced TiO_2 to enhance the absorption of visible light. In addition, black titanium dioxide has high electrical conductivity and it is recognized as a photocatalyst with good prospects. Therefore, the application potential of reducing TiO_2 in an in-plasma-catalysis process is worth exploring.

Inspired by the above ideas, we chose γ-Al_2O_3 as the carrier because of its good adsorption performance and regular morphology. The Ti^{3+} self-doped TiO_{2-x} was prepared by a simple $NaBH_4$ reduction process. We then investigated and compared the degradation effect of TiO_2 before and after reduction in the plasma-driven catalysis process, and the discharge characteristics before and after the catalyst was placed in the discharge interval were analyzed to prove the synergy between the plasma and the catalyst. In order to further explain the reaction phenomena, we combined a variety of characterization and analysis methods to compare the physical and chemical properties of the TiO_2 before and after reduction. The crystalline form and morphology changes of TiO_{2-x} before and after the reaction were explored to verify the stability of the process. Meanwhile, ion chromatography was used to analyze the surface products of the catalyst after discharge, and a possible mechanism was proposed.

2. Experiments

2.1 Synthesis of Ti^{3+} self-doped TiO_{2-x}

The catalysts used in this experiment include P25, TiO_2 and TiO_{2-x}. The P25 (particle size: 21 nm; purity: 99.50%) was produced by Evonik Deguset Chemical Co., Ltd, and TiO_2 (anatase; particle size: 30 m; purity: 99.98%) was produced by

Shanghai Aladdin Biochemical Technology Co., Ltd. The typical preparation process (Fig. 1) of Ti^{3+} self-doped TiO_{2-x} was as follows: first, 2.00 g of commercial TiO_2 and 4.00 g of $NaBH_4$ (AR grade; purity: 98.00%) were weighed, and both were thoroughly ground in a mortar for 15 minutes. Then, the mixture was heated to 350 °C at a heating rate of 6–7 °C min^{-1} in N_2, retained at 350 °C for 2 h, and then naturally cooled to room temperature. The calcined mixture was washed three times with a large amount of deionized water to remove unreacted $NaBH_4$ and washed three times with absolute ethanol (AR grade) to prevent agglomeration. The mixed liquid was vacuum dried at 60 °C after decompression filtration to obtain black TiO_{2-x}.

2.2 In-plasma-catalysis procedure for degrading NO_x

A schematic diagram of the in-plasma-catalysis procedure for degrading NO_x is shown in Fig. 2(a). N_2 (volume fraction: 99.999%), O_2 (volume fraction: 99.999%) and NO (volume fraction: 10.000%; balanced gas: N_2) were fully mixed in certain proportions in the gas cylinder as simulated gas, and the flow rate of the simulated gas was controlled by a mass flow control valve (MFC300, Wuxi Aitoly Electric Technology Co., Ltd.) at 1.50 L min^{-1}. Based on the flue gas composition in industry,[33] the N_2 was considered as the background gas and the $N_2/O_2/NO$ system was considered as the simulated gas in this work. As shown in Table 1, the NO concentration was controlled at 500 ± 10 ppm, the volume percentage of oxygen was controlled at 6 ± 0.05%, and the gas temperature at the inlet of the reactor was controlled at 25 °C, respectively. It is worth noting that before the start of the reaction, we first introduced N_2 for one hour to remove the residual air in the reactor. As shown in Fig. 2(b) and Table 2, the dual dielectric coaxial DBD reactor used a quartz electrode (outer diameter: 12.00 mm) as a high-voltage electrode, the unilateral discharge gap of the device was 4 mm, and the outer quartz tube (outer diameter: 25.00 mm) was covered with a wire mesh with a length of 150.00 mm as a ground electrode. The plasma reactor was driven by a modulated pulse power system (CTP-2000K, Nanjing Suman Electronics Co., Ltd.), the output voltage range was 0–30 kV, the input pulse frequency was set to 75 Hz, and the input pulse duty cycle was set to 70%. In this experiment, the energy density (J L^{-1}) was controlled by adjusting the output voltage. The current value, voltage value and waveform during the reaction were recorded by a digital oscilloscope (TBS1000B, Tektronix Technology Co., Ltd.). The output power (J s^{-1}) in the reaction process was calculated using the area of the voltage–charge Lissajous figure.[34] In order to evenly put the catalyst into the reactor, 1.50 g of catalyst and 15.00 g of commercial γ-Al_2O_3 pellets (particle size: 2 mm) were
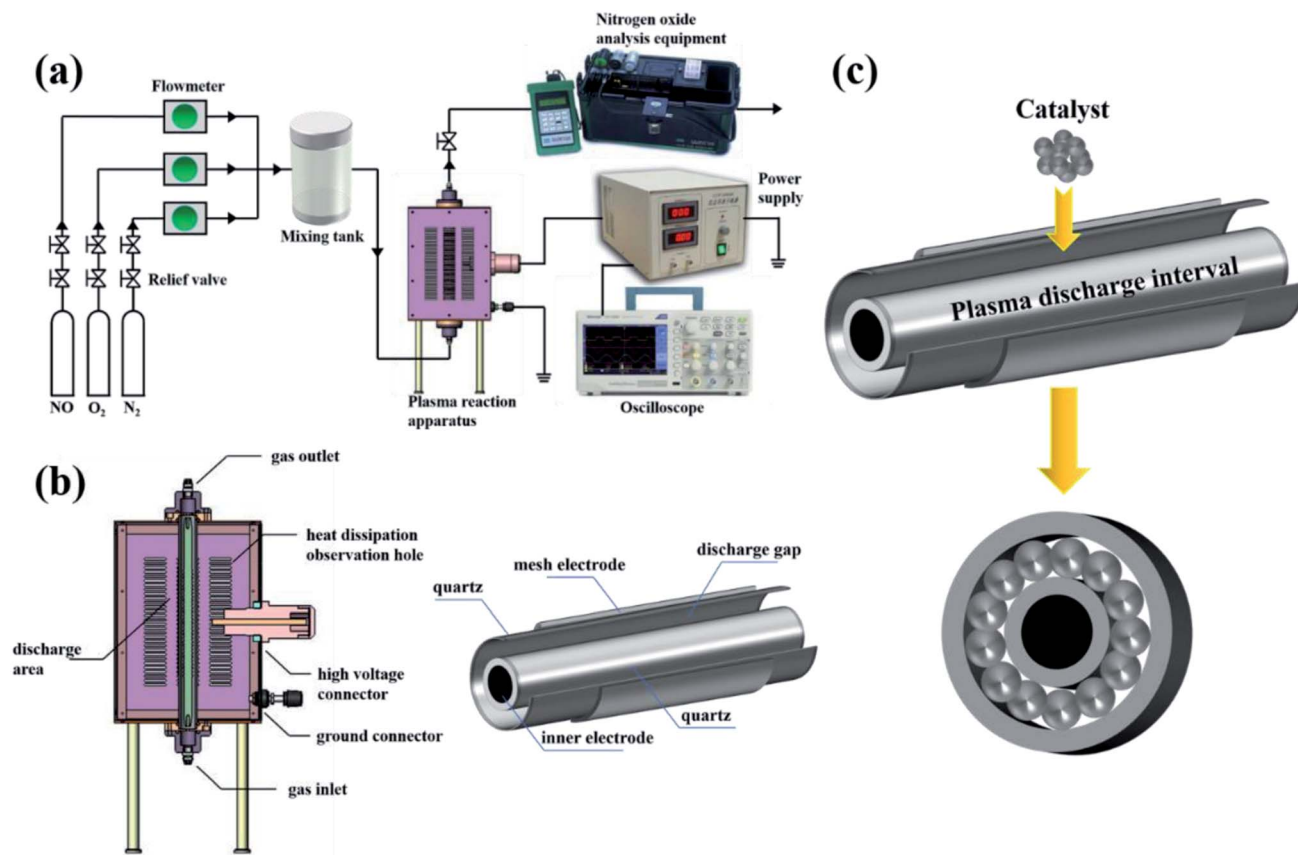
Fig. 2 (a) Schematic diagram of the in-plasma-catalysis procedure for degrading NO_x. (b) Schematic diagram of a coaxial dual medium DBD reactor. (c) Schematic diagram of catalyst filling into the discharge interval.

Table 1 Gas composition of inlet gas in the experiment

N_2 (L min^{-1})	O_2 (L min^{-1})	NO (mL min^{-1})	O_2 (%)	NO (ppm)	NO_2 (ppm)	NO_x (ppm)	T (°C)
1.365	0.135	13.50	5.96	503	271	774	25.0

mixed vigorously in a constant temperature oscillator (TS-100B, Shanghai Jiecheng Experimental Instrument Co., Ltd.) for 10 minutes. In this way, the catalyst could be better supported on the γ-Al_2O_3 pellets, and the process of filling the catalyst into the DBD discharge interval is shown in Fig. 2(c).

Table 2 Parameters of the coaxial dual medium DBD reactor

Parameters of reactor	Accurate value
Material of outer medium	Quartz
Outer diameter of outer medium (mm)	25.00
Inner diameter of outer medium (mm)	20.00
Material of inner medium	Quartz
Outer diameter of inner medium (mm)	12.00
Inner diameter of inner medium (mm)	7.50
Material of inner electrode	Stainless steel
Outer diameter of inner electrode (mm)	7.50
Unilateral discharge gap (mm)	4.00
Length of discharge interval (mm)	150.00
Reactor volume (cm^3)	60.28

During the reaction, the concentrations of NO, NO_2, and NO_x and the oxygen volume fraction were measured by a flue gas analyzer (KM9206, Kane International Limited, UK). Since a thermocouple would interfere with the discharge phenomenon in the reactor, the temperature of the reaction process was measured by an infrared thermometer (AS700, Xima Technology Co., Ltd.). The levels of NO_2^- and NO_3^- on the surface of the catalyst were measured by ion chromatography (Dionex ICS-600, ThermoFisher Scientific).

2.3 Characterization of the catalyst

X-ray diffraction (EMPYREAN, PANalytical B.V.) was used to characterize the crystal form and phase of the catalyst. The target source was Cu Kα radiation ($\lambda = 1.540598$), and the scan was carried out between 15° and 90° at a rate of 0.4° s^{-1}. Laser Raman spectrometry (LabRAM HR, HORIBA Jobin Yvon) was used to characterize the structure of the catalyst. The excitation source wavelength was 532.17 nm and the excitation wavelength

range was 100–900 cm^{-1}. Scanning electron microscopy (ZEISS Gemini 300, Carl Zeiss AG) was used to characterize the microscopic morphology of the catalyst. X-ray photoelectron spectrometry (Thermo Scientific K-Alpha, ThermoFisher Scientific) was used to characterize the surface elemental composition, valence state distribution and valence band information of the catalyst. Ultraviolet-visible spectrophotometry (UV-3600, Shimadzu Corporation) was used to analyze the light response range of the catalyst, and the test wavelength range was 200–800 nm. BET measurement (ASAP2460, McMuritik Instruments) was used to determine the specific surface area of the catalyst, and the pore size distribution of the catalyst was calculated according to the BJH (Barrett–Joyner–Halenda) model. EPR spectrometry (MiniScope MS5000 EPR spectrometer, Freiberg Instruments) was used to measure the electron spin resonance spectrum of the catalyst.

3. Results and disscuion

The specific input energy (SIE) can be defined using eqn (1) and (2) as follows.

$$SIE = \frac{P}{Q} \tag{1}$$

$$P = \frac{1}{T} \int_0^T VI \mathrm{d}t = \frac{C_M}{T} \int_0^T V \frac{\mathrm{d}V_M}{\mathrm{d}t} = fC_M \int V \mathrm{d}V_M = fC_M S_{\mathrm{Lissajous}}^{\#} \tag{2}$$

The NO removal efficiency (E_{NO}) is defined in eqn (3).

$$E_{NO} = \frac{C_{\mathrm{in,NO}} - C_{\mathrm{out,NO}}}{C_{\mathrm{in,NO}}} \times 100\% \tag{3}$$

The concentration of NO_x is defined in eqn (4).

$$C_{NO_x} = C_{NO} + C_{NO_2} \tag{4}$$

The NO_x removal efficiency (E_{NOx}) is defined in eqn (5).

$$E_{NO_x} = \frac{C_{\mathrm{in,NO}_x} - C_{\mathrm{out,NO}_x}}{C_{\mathrm{in,NO}_x}} \times 100\% \tag{5}$$

3.1 Catalyst characterization

X-ray diffraction analysis clearly showed that the TiO_2 and reduced TiO_{2-x} were in anatase phases; the diffraction peaks at $2\theta = 25.3°, 37.8°, 48.1°, 54.1°, 54.9°, 62.7°, 68.9°, 70.2°$ and $75.1°$ corresponded to the (101), (004), (200), (105), (211), (204), (116), (220) and (215) crystal planes of anatase TiO_2, respectively (PDF card 731764, JCPDS). Commercial P25 contained a mixture of rutile and anatase phases. As shown in Fig. 3(a), the crystal form of TiO_{2-x} still well maintained its crystalline structure during the reduction process using sodium borohydride at 350 °C. It could be found that the diffraction peaks of TiO_{2-x} at 25.3°, 54.1°, and 54.9° became weaker and wider, which was caused by disorder of the crystal lattice caused by the formation of Ti^{3+} and oxygen vacancies.[35] The X-ray diffraction pattern of the reacted TiO_{2-x} further confirmed that the crystal structure of TiO_{2-x} was relatively stable during the plasma discharge process (SIE = 680.2957 J L^{-1}). Raman spectroscopy is an effective means to compare the structural differences of P25, TiO_2 and TiO_{2-x}, as shown in Fig. 3(b). The frequencies of the Raman active modes of the three titanium dioxides were approximately 144, 198, 399, 518, and 640 cm^{-1}, which corresponded to the vibrations of the anatase phase.[36] In the range of 100–200 cm^{-1}, it could be seen that the E_g mode of the reduced TiO_{2-x} appeared at 150 cm^{-1}, which was higher than the frequency of commercial TiO_2 (144 cm^{-1}) because of the presence of oxygen vacancies.[36]

The morphologies and microstructures of the samples were investigated using scanning electron microscopy (SEM) and energy dispersive X-ray (EDX) analysis. As shown in Fig. 4, it was observed that the TiO_2 samples before and after reduction were all composed of spherical particles, which showed no obvious deformation after reduction. The EDX analysis revealed a decrease in O content of TiO_{2-x}, which was attributed to the existence of oxygen vacancies. It should be mentioned that the
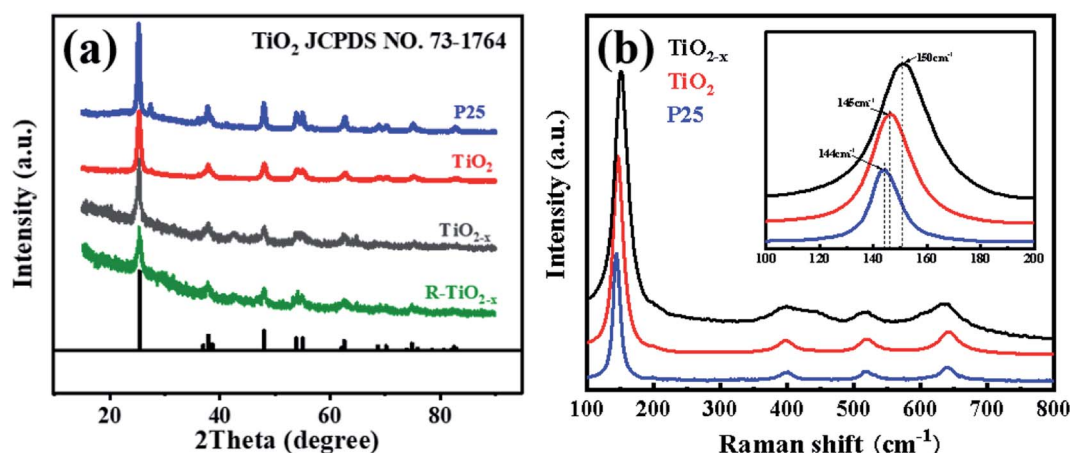

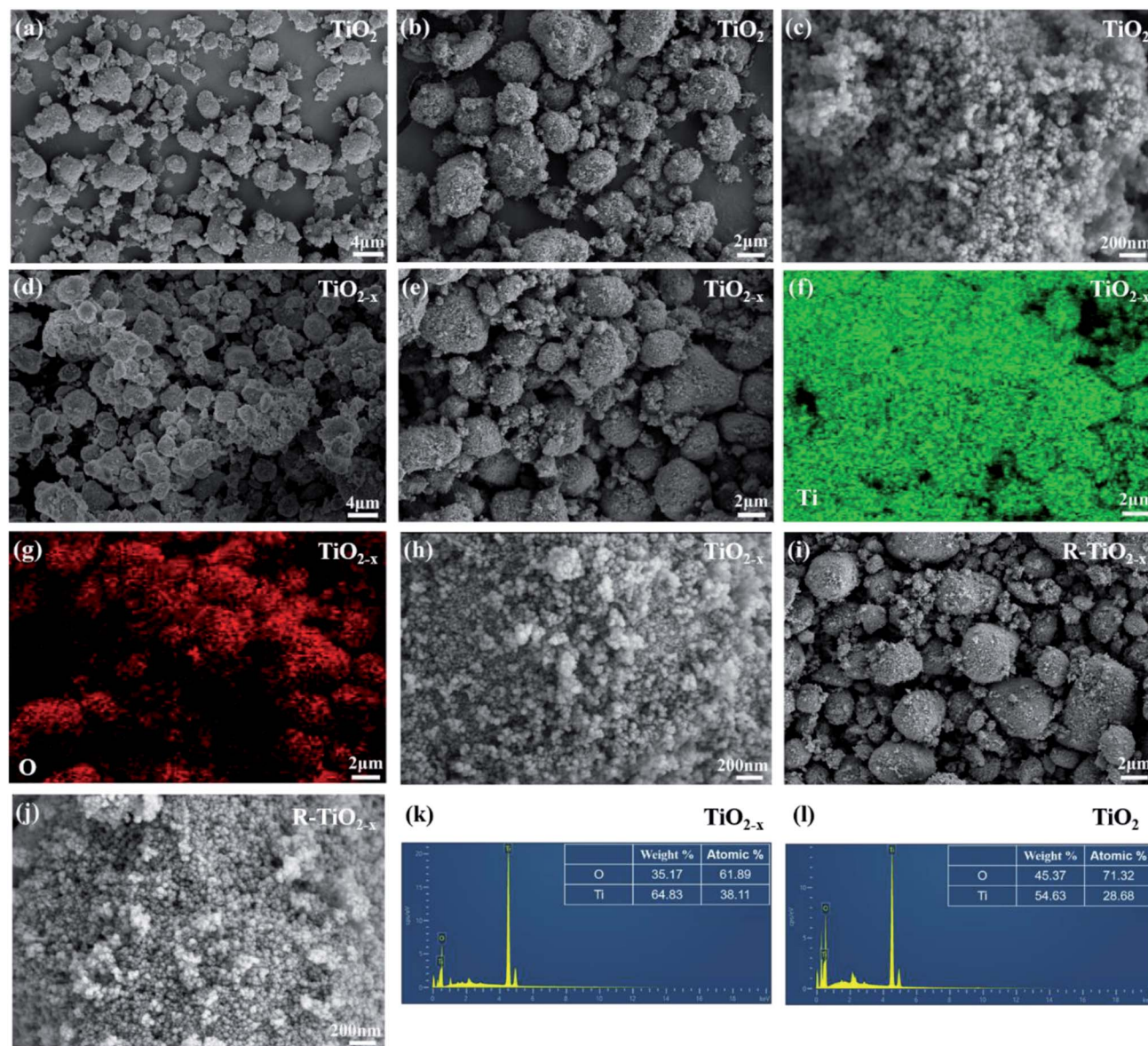Fig. 3 (a) XRD patterns of the catalysts. (b) Raman spectra of the catalysts.

Fig. 4 (a−c) SEM images of TiO_2. (d−h) SEM images of TiO_{2-x}. (f) Ti elemental mapping images of TiO_{2-x}. (g) O elemental mapping images of TiO_{2-x}. (i and j) SEM images of reacted TiO_{2-x}. (k) EDX images of TiO_{2-x}. (l) EDX images of TiO_2.

morphology of the reacted TiO_{2-x} remained spherical, as shown in Fig. 4(i), which confirmed the morphological stability of TiO_{2-x} during the DBD discharge process.

The XPS survey scan further confirmed the successful doping of Ti^{3+}. Deconvolution of the Ti 2p profile of TiO_2 (Fig. 5(d)) revealed two peaks at 459.0 and 465.0 eV, respectively, which indicated the presence of Ti^{4+}. On the other hand, the Ti 2p spectrum (Fig. 5(c)) of TiO_{2-x} exhibited two new peaks (458.4 and 463.9 eV), which were attributed to the successful implantation of Ti^{3+}. Deconvolution of the O 1s profile of TiO_{2-x} (Fig. 5(e)) revealed four peaks at 529.4, 530.0, 530.9 and 532.2 eV, which corresponded to Ti^{3+}–O, Ti–OH, surface defects and peroxide groups, respectively, which indicated that there were oxygen vacancies in TiO_{2-x}. Due to the limited methods for quantitatively determining the concentration of oxygen

vacancies,[37] we focused on qualitatively verifying the existence of oxygen vacancies in TiO_{2-x}. It is worth noting that research studies[38,39] reported the binding energy of N 1s of N-doped TiO_{2-x} to be around 400.0 eV. As shown in Fig. 5(a), the XPS spectrum of TiO_{2-x} verified that the preparation method adopted in this work did not lead to the doping of N, and N_2 played the role of providing a protective atmosphere during the preparation process.

Compared with commercial TiO_2, the reduced TiO_{2-x} has considerable photoresponse characteristics in the ultraviolet-visible light spectrum. As shown in Fig. 6(a), the absorption peak in the range of 400–800 nm of TiO_{2-x} was significantly higher than that of the other two catalysts, which was consistent with the black color of TiO_{2-x}. Meanwhile, considerable visible light absorption also provided direct proof that TiO_{2-x}

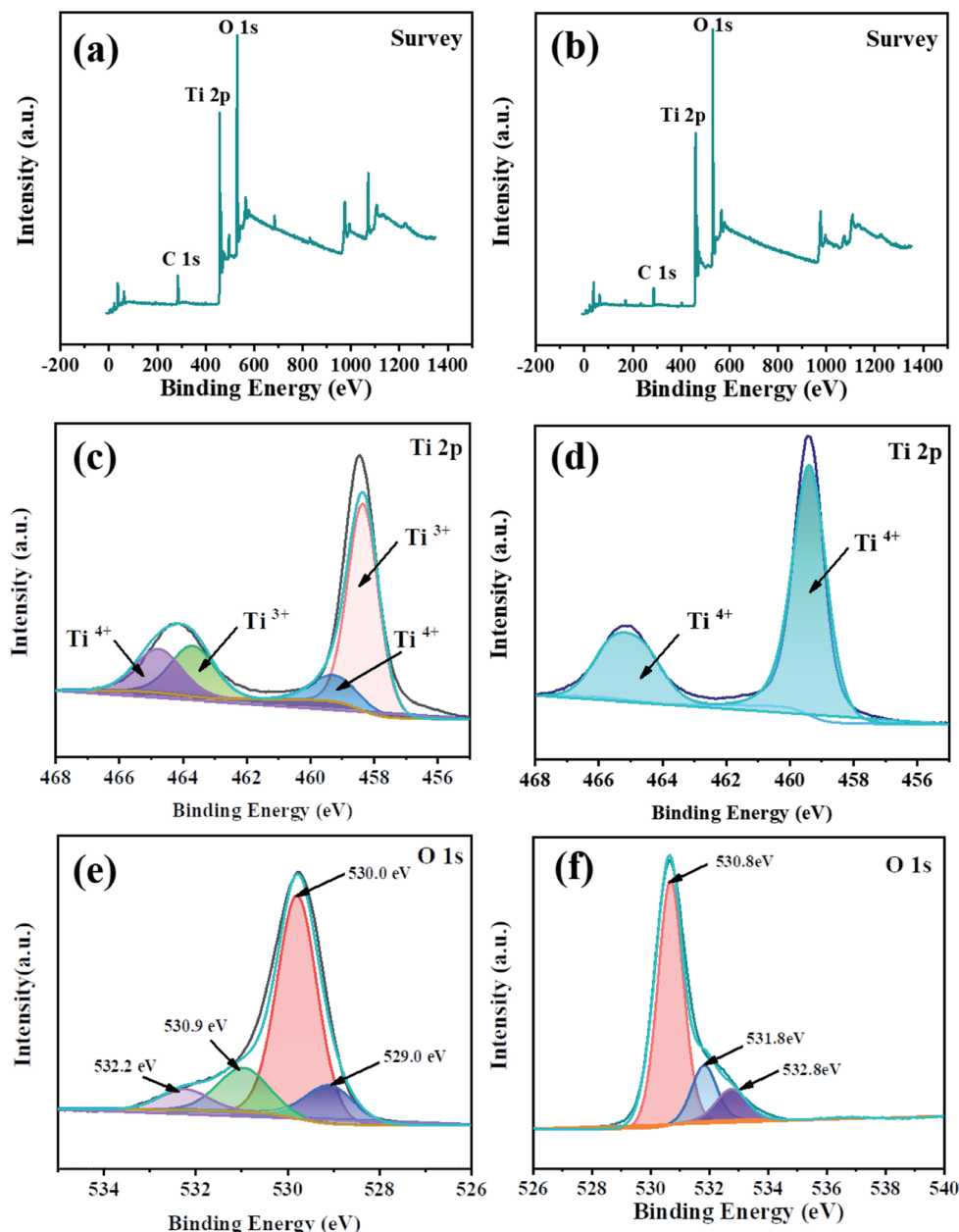Fig. 5 XPS spectra of the catalysts (a, c, e: TiO_{2-x}; b, d, f: TiO_2).

contained a large number of oxygen vacancies.[40] The band gap of TiO_{2-x} was found to be 2.98 eV, which was lower than that of commercial TiO_2 (3.29 eV), as shown in Fig. 6(b). This was due to the variation induced by the self-doped Ti^{3+} that increased an isolated energy level in the band gap of TiO_2, rather than shifting the valence band or conduction band position, which is caused by doping other atoms.[41]

The N_2 adsorption–desorption isotherms and pore size distributions of the original TiO_2 and reduced TiO_{2-x} are shown in Fig. 7. The isotherms of TiO_2 and TiO_{2-x} are both type IV isotherms with H2-type hysteresis loops, and the capillary condensation phenomenon under higher pressure proved that both catalysts are mesoporous materials. According to the BJH

(Barrett–Joyner–Halenda) model, the pore size distribution and specific surface area of the catalysts were calculated (Table 3). It was found that the pore size distributions of TiO_2 and TiO_{2-x} both mainly located in the range of 2–50 nm, indicating that both of the materials possess mesoporous structures. Additionally, the specific surface areas of the two materials were relatively similar, which corresponded well with the SEM results, implying that the physical structure remained basically unchanged after reduction treatment.

The electron paramagnetic resonance (EPR) spectrum was used to further identify the existence of Ti^{3+} and oxygen vacancies, as shown in Fig. 8(a). According to the spectrum, TiO_{2-x} produced strong signals at $g = 1.991$, 1.974 and 1.923. In
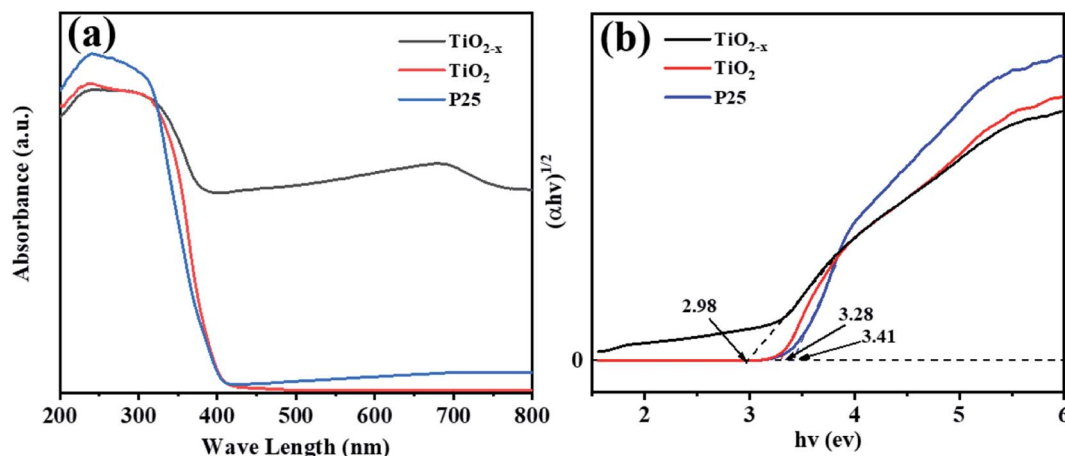
Fig. 6 UV-vis spectra of P25, TiO_2 and TiO_{2-x}.

Table 3 Specific surface area and pore volumes of the catalysts

	TiO_2	TiO_{2-x}
Specific surface area (m^2 g^{-1})	105.2569	101.1016
Pore volume (cm^3 g^{-1})	0.2960	0.3367

contrast, the EPR spectra of the unreduced TiO_2 and P25 did not produce strong paramagnetic signals. For TiO_{2-x}, the signal of $g = 1.991$ may come from oxygen vacancies, which arose due to the removal of oxygen atoms from the lattice of TiO_2 during the reduction of TiO_2.[42] The signals generated at $g = 1.974$ and $g = 1.923$ may be caused by electrons trapped by the lattice Ti^{3+}.[43] It is worth mentioning that the samples characterized were stored at room temperature for two months without any fading phenomenon and still showed strong paramagnetic signals, indicating the stability of Ti^{3+} inside TiO_{2-x}.

3.2 Discharge characteristics

Micro-discharges formed in the pores of the catalyst in the in-plasma-catalysis process, thereby affecting the discharge

process. It is worth noting that the discharge brightness of γ-Al_2O_3 and the other catalysts filled into the reactor showed an obvious decrease, which was due to the shortening of the discharge gap by the spherical medium. In this case, the filamentary discharge mode was transformed into a combination of the particle surface discharge mode and space gap filamentary discharge mode.[44] As shown in Fig. 9(a), compared with the discharge current of the empty tube, the discharge current signals under the co-operation of the catalysts were significantly enhanced. It is noted that the dielectric barrier discharge reactor was equivalent to a capacitor, and the discharge characteristics were mainly affected by the dielectric barrier material, the discharge gap, and the relative dielectric constant of the filling medium.[45] The dielectric constants of commercial TiO_2 (anatase) and γ-Al_2O_3 were 48 and 12.6, respectively. Therefore, the catalysts containing TiO_{2-x} accumulated more charges on the surface of the dielectric barrier, thereby enhancing the entire electric field.[46] Moreover, as shown in Fig. 9(b), the discharge output power measured by the V–Q Lissajous method[34] showed that the discharge efficiency after the introduction of the catalyst was higher than that without the
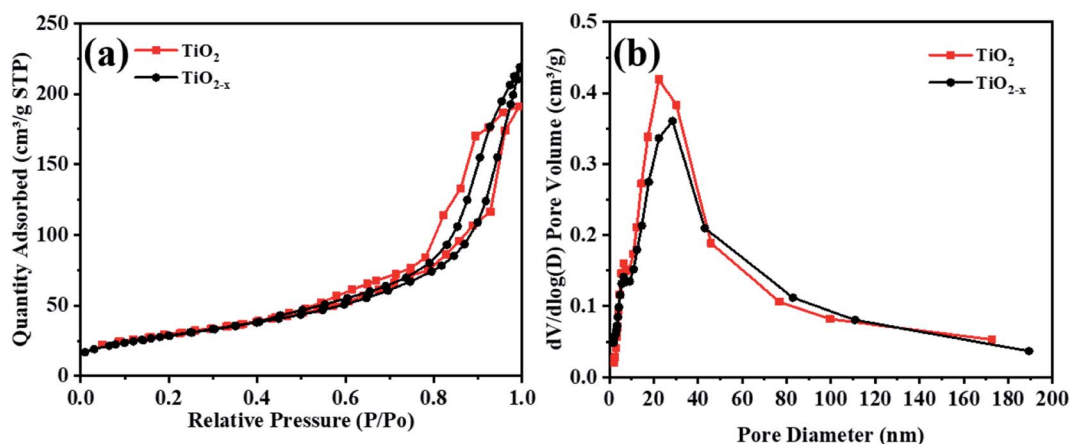

Fig. 7 BET analysis of TiO_2 and TiO_{2-x}.

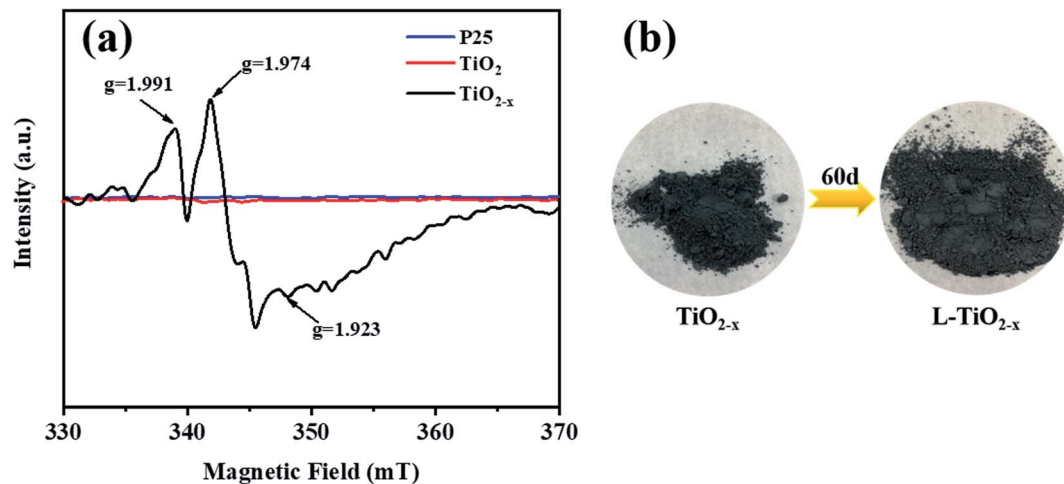**Fig. 8** (a) EPR pattern of P25, TiO_2 and TiO_{2-x}. (b) Physical picture of the color of TiO_{2-x} changing over time.

introduction of the catalyst. This indicated that with the introduction of the titanium-based catalyst, most of the applied voltage was used for gap discharge during the plasma discharge process under the condition of a certain input power.

3.3 Effect of NO_x degradation by the catalyst

The performance of the catalysts was evaluated by an experiment using the in-plasma-catalysis procedure. First of all, regardless of whether there were catalysts in the plasma, the degradation efficiency showed a positive correlation with the specific input energy. This was due to the high electron density at high power, which led to an increase in the frequency of ionization and decomposition of NO_x. The effect of introducing four kinds of catalysts to degrade NO_x is shown in Fig. 10. $TiO_{2-x}/\gamma\text{-}Al_2O_3$ exhibited an 86.69% NO degradation effect (average in 1 h) and 84.84% NO_x degradation effect (average in 1 h) at 401.27 J L^{-1}, which was better than that of $TiO_2/\gamma\text{-}Al_2O_3$ (72.14% NO degradation effect and 73.99% NO_x degradation effect at 401.27 J L^{-1}). Moreover, the empty tube reactor without

any catalysts had the worst degradation effect on NO and NO_x, where the higher oxygen content contributed to the not expected re-production of NO and NO_x, delivering degradation efficiencies (SIE = 401.27 J L^{-1}) of 2.91% and 26.00%, respectively. We believe that the main reason for the optimal degradation effect of TiO_{2-x} may be that its lower band gap made it easier to excite, thus the catalytic effect of TiO_{2-x} exceeded that of the typical TiO_2. Meanwhile, its adsorption ability of ultraviolet light and visible light in a wider wavelength range made it more likely to generate abundant "electron holes" and ˙OH to oxidize NO_x. In consideration of the similar morphology and crystal type of TiO_{2-x} and TiO_2, we explain the promoted NO_x oxidation by TiO_{2-x} as due to the high concentration of oxygen vacancies and Ti^{3+}. Combined with the absorption of $\gamma\text{-}Al_2O_3$, TiO_{2-x} synergized with plasma to achieve an improved NO_x degradation effect.

In order to further test the feasibility of the DBD synergy with TiO_{2-x} in practical operation, a long-term cyclic degradation of NO_x performance test was carried out. TiO_{2-x} could achieve a long lasting and efficient degradation of NO_x through water
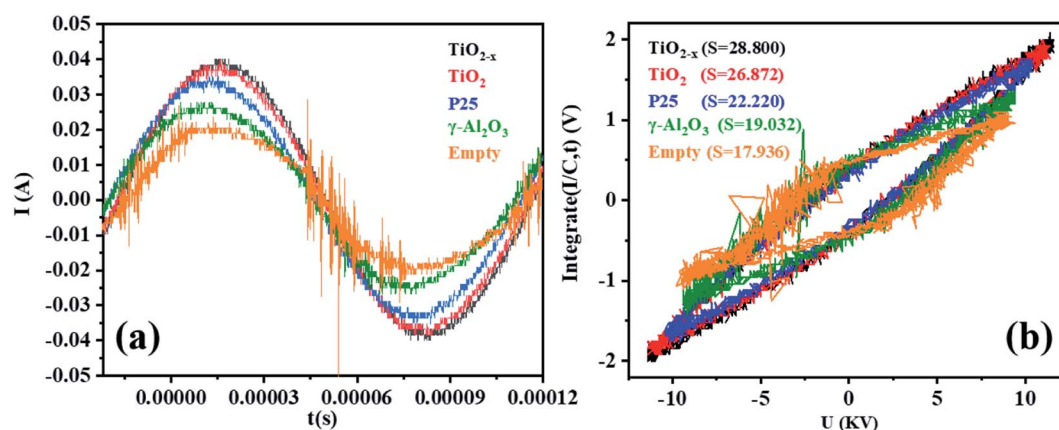

Fig. 9 (a) Current–time curves of different catalysts in a single discharge cycle in the DBD reactor (single cycle). (b) Lissajous figures of different catalysts in the DBD reactor (single cycle).
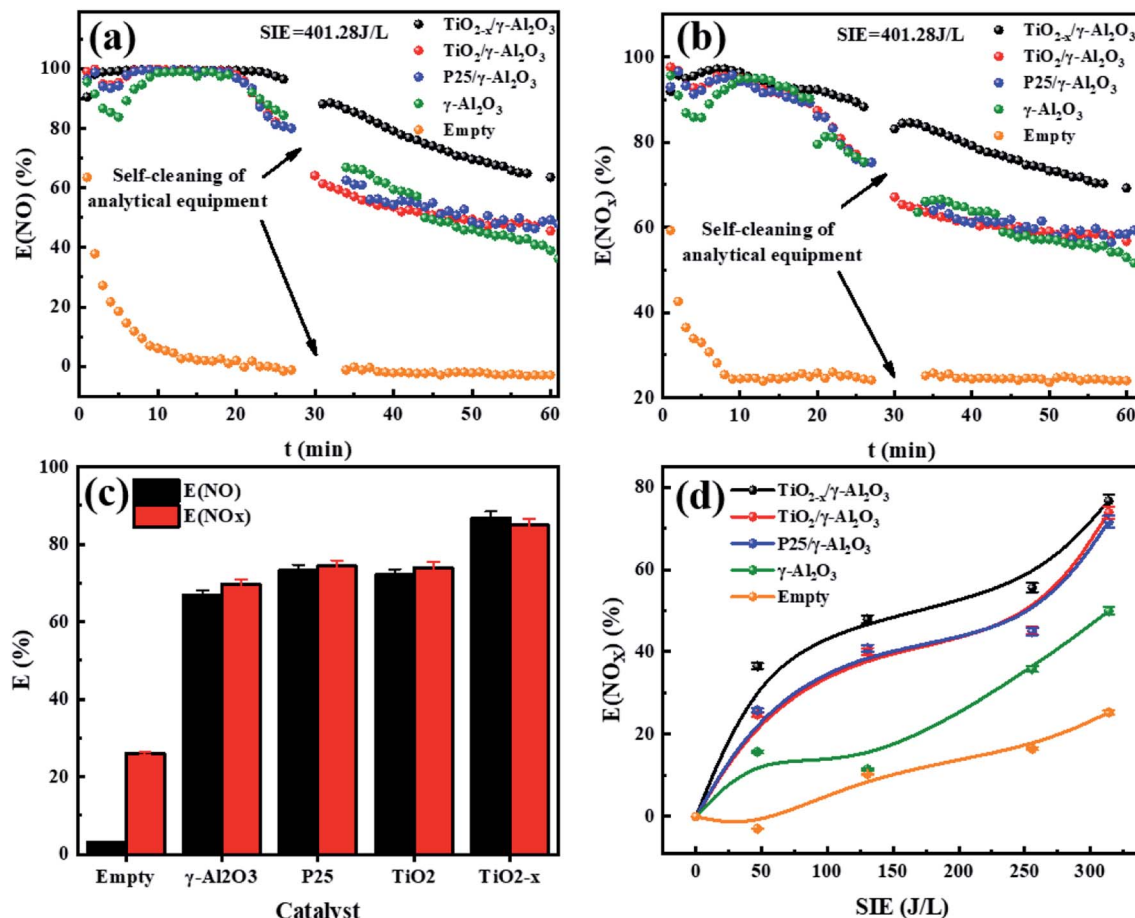
Fig. 10 (a) Real-time monitoring of NO degradation by plasma synergized with different catalysts (SIE = 401.28 J L^{-1}). (b) Real-time monitoring of NO_x degradation by plasma synergized with different catalysts (SIE = 401.28 J L^{-1}). (c) 1 h average degradation rate of different catalysts (SIE = 401.28 J L^{-1}). (d) Different kinds of catalysts degrade NO_x under different specific input energies.

washing regeneration, as shown in Fig. 11(a). Ion chromatography (IC) was applied to measure the products accumulated on the catalyst surface during the degradation of NO_x. As shown in Fig. 11(b), the main products on the catalyst surface were NO_2^-

and NO_3^-. It was observed that the change trend of NO_2^- and NO_3^- contents on the surface of different catalysts was consistent with that of the NO_x degradation effect. Herein, the degradation products of the empty tube were detected by
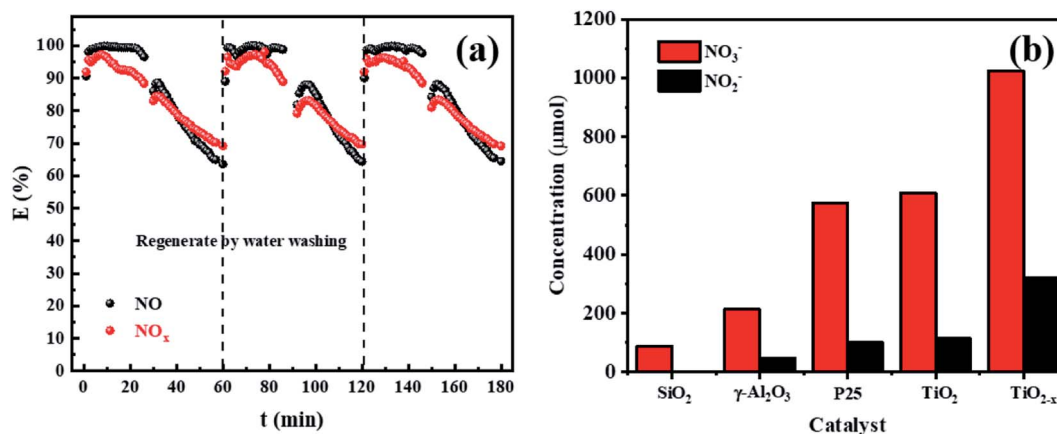

Fig. 11 (a) Long-term cyclic degradation of NO_x performance test of TiO_{2-x}. (b) Levels of NO_3^- and NO_2^- on the surface of different catalysts after discharge.
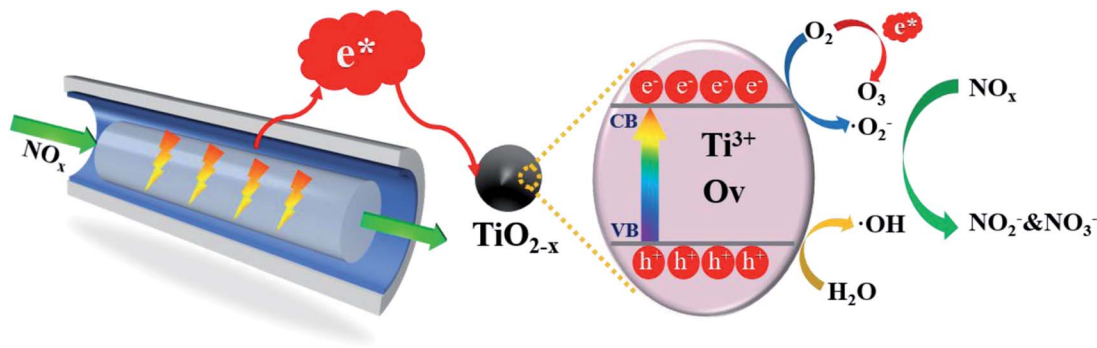
Fig. 12 Schematic diagram of the reaction mechanism of the catalytic degradation of NO$_x$ by.

introducing glass beads (SiO$_2$) into the discharge interval, and it could be observed that the NO$_3^-$ content on the surface was very low and the presence of NO$_2^-$ was not detected. For the in-plasma-catalysis system, it could be observed that the content of NO$_3^-$ and NO$_2^-$ on the surface of the Ti-based catalyst was higher than that of γ-Al$_2$O$_3$ during the discharge process, which confirmed that the photocatalyst containing TiO$_{2-x}$ was activated in the plasma field to achieve the deep oxidation of NO$_x$. Previous researchers[47] have pointed out that the intensity of ultraviolet rays generated during the plasma discharge process is basically insufficient to excite the photocatalytic process. Meanwhile, Chen et al.[23] believed that one of the key factors in the process of plasma-assisted N-type semiconductor catalysis was the forbidden band width of the catalyst. Thus, TiO$_{2-x}$ has a lower forbidden band gap that positively accelerates the catalysis process of the plasma-assisted N-type semiconductor.

3.4 Mechanism of NO$_x$ degradation

3.5.1 TiO$_{2-x}$ driven by low-temperature plasma. On the basis of the above discussion, a possible reaction mechanism for the in-plasma-catalysis process achieved by TiO$_{2-x}$/γ-Al$_2$O$_3$ is shown in Fig. 12. Firstly, the plasma provided a large number of high-energy electrons, which excited TiO$_{2-x}$ to generate electron–hole pairs (e$^-$ and h$^+$) through the "pseudo-photocatalytic" process. Electrons and holes respectively reacted with H$_2$O/O$_2$ on the surface of TiO$_{2-x}$ to generate large amounts of ·OH and ·O$_2^-$. The NO absorbed on the surface of TiO$_{2-x}$ was firstly oxidized to NO$_2$ by the generated ·OH, and then to NO$_2^-$ and NO$_3^-$. Meanwhile, the NO$_2$ adsorbed on the surface of TiO$_{2-x}$ was directly oxidized to NO$_2^-$ and NO$_3^-$ by the generated ·OH. In addition, a certain concentration of O$_3$ was produced during the discharge process, which further promoted the oxidation of NO$_x$. The importance of ·OH was emphasized in this work, however no water was introduced into the experimental process. It is worth noting that the air tightness of the reaction device was good, and the catalysts were all dried. We believe that the water in the reaction process may come from the cylinder gas, or surface adsorbed water on the catalysts or the reactor.[48–50] The XPS spectrum of Fig. 5(e) also supported the possibility of adsorbed water on the catalyst surface.[51] It is worth noting that the introduction of TiO$_{2-x}$/γ-Al$_2$O$_3$ into the in-plasma-catalysis process improved the electric field intensity

and energy density of the plasma discharge to a certain extent, thereby increasing the average electron energy and making TiO$_{2-x}$ easier to excite.

4.   Conclusions

Ti^{3+} self-doped TiO$_{2-x}$ was successfully constructed through a simple and gentle NaBH$_4$ reduction process, and the existence of Ti^{3+} and oxygen vacancies was confirmed by a variety of characterization methods. Compared with the plasma alone, the introduction of TiO$_{2-x}$/γ-Al$_2$O$_3$ into the system effectively improved the discharge intensity and energy efficiency of the reactor, achieving a considerable degradation effect on NO$_x$. The in-plasma-catalysis process achieved by TiO$_{2-x}$/γ-Al$_2$O$_3$ exhibited 86.69% NO and 84.84% NO$_x$ degradation effects at 401.27 J L^{-1}. It was confirmed that TiO$_{2-x}$ has a smaller forbidden band width, and more abundant Ti^{3+} and oxygen vacancies, enabling it to exhibit a better and more stable degradation effect when compared to the characteristics of TiO$_2$ before and after reduction. Moreover, the rapidly increased levels of NO$_3^-$ and NO$_2^-$ on the surface of the catalysts further confirmed the superiority of TiO$_{2-x}$. The innovative combination of plasma and Ti^{3+} self-doped TiO$_{2-x}$ should inspire more opportunities for low-temperature NO$_x$ degradation. Furthermore, herein, a facile synthesis procedure of TiO$_{2-x}$ was provided for industrial applications.

Nomenclature

P	Discharge power, W
T	Discharge cycle, s
V	Discharge voltage between electrodes, V
I	Discharge current, A
C_M	Additional capacitance, F
V_M	Voltage at both ends of the additional capacitor, V
f	Power frequency, Hz
$S_{Lissajous}$	Area of Lissajous figure
SIE	Specific input energy, J L^{-1}
Q	Gas flow, L min^{-1}
$C_{in,NO}$	NO concentration at the inlet of the reactor, ppm
$C_{out,NO}$	NO concentration at the outlet of the reactor, ppm
C_{in,NO_x}	NO$_x$ concentration at the inlet of the reactor, ppm

C_{out,NO_x} NO_x concentration at the outlet of the reactor, ppm

Conflicts of interest

There are no conflicts to declare.

Acknowledgements

References

1 D. R. Kanter and T. D. Searchinger, *Nat. Sustain.*, 2018, **1**, 544–552.

2 X. J. Liu, W. Xu, E. Z. Du, A. H. Tang, Y. Zhang, Z. Wen, T. X. Hao, Y. P. Pan, L. Zhang, Y. Zhao, J. L. Shen, F. Zhou, Z. L. Gao, Y. H. Chang, K. Goulding, J. L. Collett, Jr, P. M. Vitousek, F. S. Zhang, Y. Y. Zhang, B. J. Gu and Z. Z. Feng, *Philos. Trans. R. Soc., A*, 2020, **378**, 1–23.

3 F. Lin, Z. Wang, Z. Zhang, Y. He, Y. Zhu, J. Shao, D. Yuan, G. Chen and K. Cen, *Chem. Eng. J.*, 2020, **382**, 123030–123059.

4 X. Lu, L. Zhang, Y. Chen, M. Zhou, B. Zheng, K. Li, Y. Liu, J. Lin, T.-M. Fu and Q. Zhang, *Atmos. Chem. Phys.*, 2019, **19**, 8339–8361.

5 P. Talebizadeh, M. Babaie, R. Brown, H. Rahimzadeh, Z. Ristovski and M. Arai, *Renew. Sustain. Energy Rev.*, 2014, **40**, 886–901.

6 G. Chen, E. J. H. Cheung, Y. Cao, J. Pan and A. J. Danner, *Nanoscale Res. Lett.*, 2021, **16**, 32–40.

7 X. Huang, F. Guo, J. Chen, S. Wang, Z. Hu, L. Wang, Z. Chen and M. Liu, *IEEE Trans. Plasma Sci.*, 2016, **44**, 1341–1348.

8 Y. S. Mok, J.-O. Jo, H.-J. Lee, H. T. Ahn and J. T. Kim, *Plasma Chem. Plasma Process.*, 2007, **27**, 51–64.

9 M. A. Jani, K. Takaki and T. Fujiwara, *Rev. Sci. Instrum.*, 1998, **69**, 1847–1849.

10 V. R. Chirumamilla, W. F. L. M. Hoeben, F. J. C. M. Beckers, T. Huiskamp, E. J. M. Van Heesch and A. J. M. Pemen, *Plasma Chem. Plasma Process.*, 2016, **36**, 487–510.

11 H. Pan, Y. Guo, Y. Jian and C. He, *Energy Fuels*, 2015, **29**, 5282–5289.

12 B. S. Rajanikanth and A. D. Srinivasan, *IEEE Trans. Dielectr. Electr. Insul.*, 2007, **14**, 302–311.

13 H. Wang, J. Wang, L. Zhang, Q. Yu, Z. Chen and S. Wu, *Chem. Res. Chin. Univ.*, 2019, **35**, 1062–1069.

14 M. Zangouei and B. S. Haynes, *Plasma Chem. Plasma Process.*, 2019, **39**, 89–108.

15 A. M. Harling, D. J. Glover, J. C. Whitehead and K. Zhang, *Appl. Catal. B Environ.*, 2009, **90**, 157–161.

16 J. L. Hueso, A. R. Gonzalez-Elipe, J. Cotrino and A. Caballero, *J. Phys. Chem. A*, 2007, **111**, 1057–1065.

17 I. Jogi, E. Stamate, C. Irimiea, M. Schmidt, R. Brandenburg, M. Holub, M. Bonislawski, T. Jakubowski, M.-L. Kaariainen and D. C. Cameron, *Fuel*, 2015, **144**, 137–144.

18 T. Wang, H. Liu, X. Zhang, Y. Guo, Y. Zhang, Y. Wang and B. Sun, *Fuel Process. Technol.*, 2017, **158**, 199–205.

19 C. Shi, Z.-s. Zhang, M. Crocker, L. Xu, C.-y. Wang, C. Au and A.-m. Zhu, *Catal. Today*, 2013, **211**, 96–103.

20 Z. Chang, C. Wang and G. Zhang, *Plasma Processes Polym.*, 2020, **17**, 1–24.

21 M. Humayun, F. Raziq, A. Khan and W. Luo, *Green Chem. Lett. Rev.*, 2018, **11**, 86–102.

22 S. M. Gupta and M. Tripathi, *Chin. Sci. Bull.*, 2011, **56**, 1639–1657.

23 S. Chen, H. Wang, M. Shi, H. Ye and Z. Wu, *Environ. Sci. Technol.*, 2018, **52**, 8568–8577.

24 X. Chen, L. Liu, P. Y. Yu and S. S. Mao, *Science*, 2011, **331**, 746–750.

25 Q. Bi, X. Huang, Y. Dong and F. Huang, *Catal. Lett.*, 2020, **150**, 1346–1354.

26 T.-D. Nguyen, J. Li, E. Lizundia, M. Niederberger, W. Y. Hama and M. J. MacLachlan, *Adv. Funct. Mater.*, 2019, **29**, 1904639–1904648.

27 X. Hou, C.-W. Wang, W.-D. Zhu, X.-Q. Wang, Y. Li, J. Wang, J.-B. Chen, T. Gan, H.-Y. Hu and F. Zhou, *Solid State Sci.*, 2014, **29**, 27–33.

28 C. McManamon, J. O'Connell, P. Delaney, S. Rasappa, J. D. Holmes and M. A. Morris, *J. Mol. Catal. Chem.*, 2015, **406**, 51–57.

29 X. Wu, S. Yin, Q. Dong, C. Guo, H. Li, T. Kimura and T. Sato, *Appl. Catal. B Environ.*, 2013, **142**, 450–457.

30 A. A. Ismail and D. W. Bahnemann, *J. Phys. Chem. C*, 2011, **115**, 5784–5791.

31 J. Fang, S.-W. Cao, Z. Wang, M. M. Shahjamali, S. C. J. Loo, J. Barber and C. Xue, *Int. J. Hydrogen Energy*, 2012, **37**, 17853–17861.

32 D. Yang, Y. Sun, Z. Tong, Y. Tian, Y. Li and Z. Jiang, *J. Phys. Chem. C*, 2015, **119**, 5827–5835.

33 Z. Wang, H. Kuang, J. Zhang, L. Chu and Y. Ji, *RSC Adv.*, 2019, **9**, 5402–5416.

34 H. Jiang, T. Shao, C. Zhang, W. Li, P. Yan, X. Che and E. Schamiloglu, *IEEE Trans. Dielectr. Electr. Insul.*, 2013, **20**, 1101–1111.

35 X. Yan, Z. Xing, Y. Cao, M. Hu, Z. Li, X. Wu, Q. Zhu, S. Yang and W. Zhou, *Appl. Catal. B Environ.*, 2017, **219**, 572–579.

36 Q. Zhu, Y. Peng, L. Lin, C.-M. Fan, G.-Q. Gao, R.-X. Wang and A.-W. Xu, *J. Mater. Chem. A*, 2014, **2**, 4429–4437.

37 K. Ye, K. Li, Y. Lu, Z. Guo, N. Ni, H. Liu, Y. Huang, H. Ji and P. Wang, *TrAC, Trends Anal. Chem.*, 2019, **116**, 102–108.

38 G. Li, J. Li, G. Li and G. Jiang, *J. Mater. Chem. A*, 2015, **3**, 22073–22080.

39 K. Zhang, W. Zhou, L. Chi, X. Zhang, W. Hu, B. Jiang, K. Pan, G. Tian and Z. Jiang, *ChemSusChem*, 2016, **9**, 2841–2848.

40 X. Liu, G. Dong, S. Li, G. Lu and Y. Bi, *J. Am. Chem. Soc.*, 2016, **138**, 2917–2920.

41 S. Hoang, S. P. Berglund, N. T. Hahn, A. J. Bard and C. B. Mullins, *J. Am. Chem. Soc.*, 2012, **134**, 3659–3662.

42 X. Liu, S. Gao, H. Xu, Z. Lou, W. Wang, B. Huang and Y. Dai, *Nanoscale*, 2013, **5**, 1870–1875.

43 Z. Pei, L. Ding, H. Lin, S. Weng, Z. Zheng, Y. Hou and P. Liu, *J. Mater. Chem. A*, 2013, **1**, 10099–10102.

44 T. Butterworth and R. W. K. Allen, *Plasma Sources Sci. Technol.*, 2017, **26**, 065008–065023.

45 O. Guaitella, F. Thevenet, C. Guillard and A. Rousseau, *J. Phys. Appl. Phys.*, 2006, **39**, 2964–2972.

46 N. Lu, Y. Hui, K. Shang, N. Jiang, J. Li and Y. Wu, *Plasma Chem. Plasma Process.*, 2018, **38**, 1239–1258.

47 H.-H. Kim, Y. Teramoto, A. Ogata, H. Takagi and T. Nanba, *Plasma Chem. Plasma Process.*, 2016, **36**, 45–72.

48 S. Chen, Y. Zhou, J. Li, Z. Hu, F. Dong, Y. Hu, H. Wang, L. Wang, K. K. Ostrikov and Z. Wu, *ACS Catal.*, 2020, **10**, 10185–10196.

49 G. Dong, L. Yang, F. Wang, L. Zang and C. Wang, *ACS Catal.*, 2016, **6**, 6511–6519.

50 G. Dong, W. Ho, Y. Li and L. Zhang, *Appl. Catal. B Environ.*, 2015, **174–175**, 477–485.

51 B. Li, X. Zhu, J. Wang, R. Xing, Q. Liu, X. Shi, Y. Luo, S. Liu, X. Niu and X. Sun, *Chem. Commun.*, 2020, **56**, 1074–1077.